

Phase and texture analysis of a hydride blister in a Zr–2.5%Nb tube by synchrotron X-ray diffraction

M.A. Vicente Alvarez^{a,*}, J.R. Santisteban^a, G. Domizzi^b, J. Almer^c

^a Centro Atómico Bariloche, Laboratorio de Física de Neutrones y Reactores, Bustillo km 9.5, San Carlos de Bariloche, Río Negro 8400, Argentina

^b Centro Atómico Constituyentes, CNEA, Av. Libertador 8250, Buenos Aires 1429, Argentina

^c Advanced Photon Source, Argonne National Laboratory, Argonne, IL, USA

Received 8 October 2010; received in revised form 10 December 2010; accepted 12 December 2010

Available online 11 January 2011

Abstract

This paper presents a detailed phase and texture study within and around a hydride blister grown on the surface of a Zr–2.5%Nb pressure tube. The analysis is based on synchrotron X-ray diffraction experiments using an 80 keV photon beam and a high-speed area detector placed in transmission geometry. It was found that the blister is composed of two main phases, α -Zr and δ -ZrH, with a composition which changes locally across the blister. No location within the blister presents pure δ zirconium hydride, with a maximum of 80% for the volume fraction of δ hydride at the center of the blister. The texture observed for both phases in the original pressure tube remains essentially unaltered across the hydride blister. A detailed analysis of this texture using well-known parent–precipitate relationships shows that some selective precipitation occurs at α -Zr grains with their *c*-axis under a tensile stress, and on grains with grain boundaries favorably aligned for hydride nucleation.

© 2010 Acta Materialia Inc. Published by Elsevier Ltd. All rights reserved.

Keywords: Zr–2.5%Nb tube; Hydride blister; Texture; Residual stress

1. Introduction

Hydride blisters may form in hydride-forming metals such as Zr, Ti, Nb or U, owing to the redistribution and precipitation of dissolved hydrogen (H) in the presence of thermal and/or stress gradients [1]. The technological problem associated with the formation of macroscopic hydride blisters in zirconium-alloy pressure tubes was recognized in 1983, when a pressure tube failed in a CANDU power plant at Pickering [2]. The formation of hydride blisters also represents a technological issue for the safe storage of spent nuclear fuel [3] and for the cladding response to postulated reactor accidents [4]. Following the Pickering event, intensive research was initiated on the structural integrity of Zr-alloy tubes in the presence of localized temperature and stress gradients over cyclic or very long periods of time [5], and several experimental techniques were

developed for the controlled growth of blisters on pressure tube material, simulating different in-service scenarios [4–8]. It is accepted that the basic physical mechanism leading to the formation of a blister is the thermal diffusion of hydrogen (or deuterium) through the crystal lattice, with hydride precipitation occurring in the colder regions once the local solubility limit is exceeded. Cracks ubiquitously present in the brittle blister can propagate into the Zr matrix, and grow by a phenomenon known as delayed hydride cracking (DHC) [9]. Knowledge of the local stress fields at the crack tip is essential for calculating the DHC crack velocity, as the stress field influences H diffusion and dictates both the morphology and failure mode of the hydride precipitates. For cracks appearing near a blister–matrix interface, large macroscopic stresses add to the crack–tip stresses, owing to misfit strain that results from the $\sim 17\%$ volume expansion involved in the Zr \rightarrow hydride transformation. Such stresses is manifested metallographically through the precipitation of “sunburst” hydrides, i.e., short hydride platelets lying at the blister/matrix interface

* Corresponding author. Tel.: +54 2944 445490x5520.

E-mail address: m.a.vicente@cab.cnea.gov.ar (M.A. Vicente Alvarez).

and oriented normal to it [6]. In some cases, misfit stresses larger than the threshold stress for hydride reorientation can also exist away from the blister interface, inducing precipitation of radial hydrides in the pressure tube material [10]. Such radial hydrides are detrimental to the tube integrity, as they can accelerate the crack propagation.

Several theoretical attempts have been made to calculate the misfit stress field that appears within and around the blister [11–13]. It was recognized early that the distribution of hydride composition within the blister has a considerable effect on the resulting stress field, since the amount of volume expansion at any point within the blister is dependent on the hydrogen concentration existing at that point [11]. Depth profiles of deuterium concentrations on deuteride blisters, measured by high-energy ^3He bombardment [14], and microhardness measurements [5] showed that a blister is in fact a continuous distribution of hydride, with the hydride concentration varying steadily with depth. Maps of the hydride composition across the blister have been predicted by axisymmetric models of blister growth due to hydrogen dissolution, diffusion and precipitation in the presence of thermal gradients [15,7]. Stress analysis of the blister has also been based on axisymmetric models, assuming that isotropic volume expansion occurs at each point within the blister as a result of the phase transformation. Wallace [12] performed a thorough finite element stress analysis using the hydride composition distribution obtained from a thermal model of blister growth [15], predicting values of up to -400 MPa. A different approach has been recently taken by Singh et al. [13], who considered the blister as a semi-constrained inclusion, i.e., a single-phase solid hydride, hence adopting a step transition between the metal matrix and the blister. As a result, they predicted much larger tensile stresses (~ 1100 MPa).

Experimental values of stresses, recently measured by energy-dispersive synchrotron X-ray diffraction were ~ 300 MPa on the pressure tube surface [16]. These values suggest that Wallace's model is correct in essence, although more detailed information about the local volume changes occurring across the blister is still required. In particular, the assumption of isotropic expansion as a result of the phase transformation is likely to be incorrect. Carpenter [17] considered the apparent change in size of the hexagonal unit cell of Zr as a result of the phase transformation, finding that transformation to δ zirconium hydride involves an expansion of 7.2% along the $[0\ 0\ 0\ 1]$ direction, but only 4.58% along the $[11\text{--}20]$ direction, perpendicular to it. Provided pressure tubes display a crystallographic texture with most of the $(0\ 0\ 0\ 1)$ basal plane normals near the tube hoop direction, it is expected that the formation of a blister would involve a greater expansion along the hoop direction than along the axial direction. This limitation of the model was acknowledged by Wallace [12], who suggested that anisotropic expansion could have a significant effect on the blister stresses.

Both the theoretical and experimental estimations of stresses existing within the blister are much more uncertain

than those in the metal around it, owing to the intrinsic complexity of the blister mechanical properties and the possibility of crack formation, which may relax stresses. The blister is a varying mixture of a relatively isotropic hydride and a quite anisotropic metal, so its mechanical properties change continuously between these two extremes [5]. Compression tests on hydrides produced from both iodide zirconium [18,19] and Zr–2.5%Nb [20] have shown that both the yield strength and Young's modulus of solid zirconium hydrides strongly depend on hydride concentration. Besides complicating the theoretical models referred above, this also poses serious difficulties to diffraction-based stress measurement techniques, because the parameters relating the measured strains to stresses must be locally defined at each measurement position.

Recently, the high spatial resolution and count rate offered by synchrotron X-ray diffraction has furthered understanding of important aspects of hydrides' behavior in Zr alloys, such as precipitation and fracture at crack tips [21–23], kinetics of dissolution and precipitation [24,25] and mechanical response of precipitates to external loads [26,27]. This paper reports synchrotron X-ray experiments performed on a hydride blister grown on a Zr–2.5%Nb pressure tube, with the aim of characterizing the local variation in crystallographic phases and texture across the blister. The experiments were conducted at the 1-ID beamline at APS, Argonne National Laboratory, using a highly collimated beam and an area detector placed in transmission geometry. Profiles of hydride concentration were obtained with a spatial resolution of 0.3 mm. The crystallographic texture of both Zr and zirconium hydride phases were determined from an analysis of intensity variations around the Debye ring, using a novel algorithm presented in this paper. The complete orientation distribution function (ODF) for zirconium hydride in pressure tube material is presented here for the first time. The hydride ODF is explained in terms of the transformation of a small number of texture components representing the α -Zr ODF for pressure tube material.

2. Samples

A test piece was cut from a commercial Zr–2.5%Nb pressure tube. The sample was charged to a hydrogen concentration of 160 wt.ppm by gas charging at 320 °C using a Sieverts-type device. After that, the specimen was kept at 400 °C for 1 h, in order to obtain a uniform hydrogen distribution without affecting the microstructure of the material. Several coupons with dimensions of 15 mm, 10 mm and 4 mm along the axial, hoop and radial directions, respectively, were machined out from this section, as indicated in Fig. 1a. A blister was produced on the outer surface of each sample by a localized thermal gradient, obtained by pressing an aluminum cold finger (2.2×10 mm along the hoop and axial directions, respectively), while the sample was kept in an electric furnace. Details about the experimental device can be found in Ref. [7].

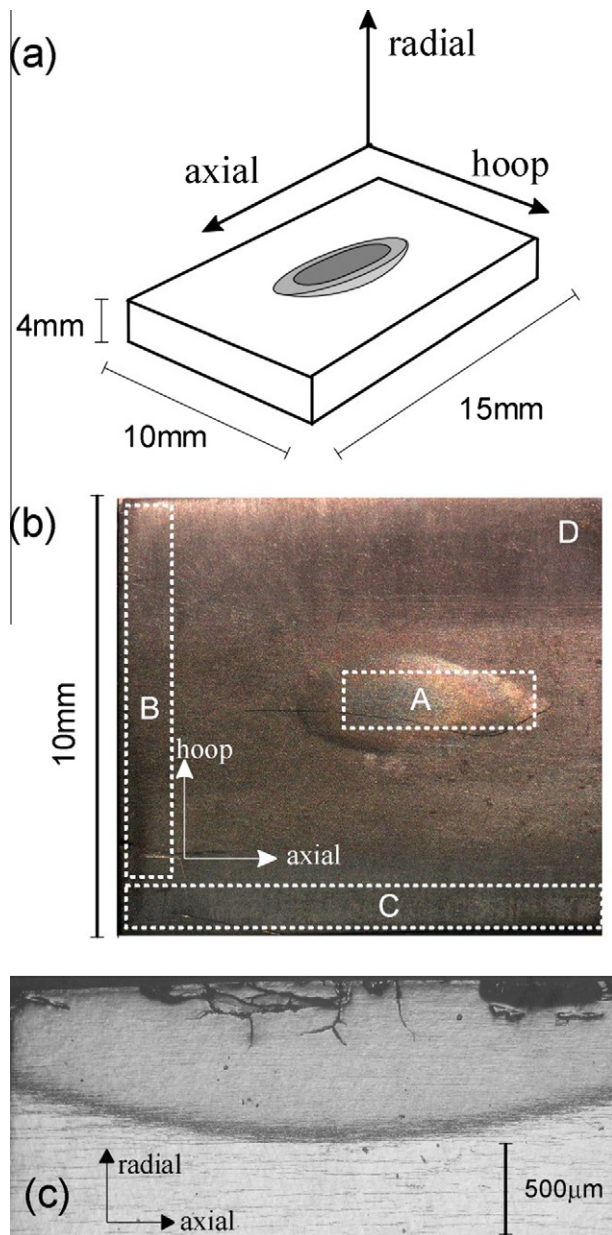


Fig. 1. Top: Schematic representation of the sample, a pressure tube section containing a hydride blister. Middle: Photograph of the sample top surface prior to sectioning into specimens A, B, C and D, as indicated in the figure. Bottom: Optical micrograph of cross section of specimen A. (For interpretation of the references to colour in this figure legend, the reader is referred to the web version of this article.)

Blisters were grown for several furnace temperatures (300–365 °C) and for different treatment times (400–3400 h). Experiments performed on a blister grown with the furnace at 320 °C over a period of 1650 h are presented here. Fig. 1b is a photograph of the actual specimen, showing that the blister size at the surface is ~5.5 mm and 2 mm along the axial and hoop directions, respectively. For the X-ray experiments, a small coupon containing most of the blister was cut out from the specimen by electro-discharge machining, as indicated in the figure by the dotted rectangle labeled “A”. So sample A was ~1.25 mm and

4 mm along the hoop and axial directions, respectively, and extended through the whole thickness along the radial direction. For such a small specimen, the blister is largely (but not completely) relieved from the macroscopic stresses exerted by the surrounding metal matrix. Experiments performed on a companion sample containing a blister under such macroscopic stresses are presented in Ref. [16]. Two extra coupons (labeled “B” and “C” in the figure) were also machined out from the specimen in order to study the material far from the hydride blister, while sample D consists of the remains of the original specimen.

Fig. 1c displays the cross section of the blister on the axial–radial plane, from a destructive examination performed at the center of sample A following the X-ray experiments. Below the surface, the blister has a semi-ellipsoidal shape up to a maximum depth of ~750 μm from the tube outer surface. Several cracks are clearly visible on the blister surface. Outside the blister, hydrides appear as horizontal parallel lines on the white background corresponding to the metal matrix. The interface between the blister, and the metal matrix appears as a darker region with thickness ~90 μm.

3. Measurement set-up

X-ray diffraction experiments were conducted at beamline 1-ID of the Advanced Photon Source at Argonne National Laboratory [28]. The beamline was used in the Debye–Scherrer transmission geometry, with a monochromatic beam of 0.15 Å wavelength (80 keV) and a size of (300 × 300) μm²; in conjunction with a high-speed charge coupled device (CCD) area detector composed of 2048 × 2048 pixels with 200 × 200 μm² size located at 1948 mm from the sample. This geometry allows a number of full diffraction rings to be recorded within a very short time (~1 s), providing information that is averaged over the full thickness of the sample. The use of a large sample–detector distance improves the angular resolution of the area detector, allowing the small distortions of Debye rings caused by the presence of internal and/or macroscopic stresses to be determined.

Debye ring images for the hydrogen-charged pressure tube material were taken for the incident X-ray beam aligned to the three principal axes of the tube. Details of the corrected CCD images are shown in Fig. 2a. Each image is the average of 10 expositions to improve statistics. Samples B, C and D were used for the incident beam along the axial, hoop and radial directions, respectively. Determination of the crystallographic texture for both the Zr and hydride phases was based on a thorough analysis of these three images. The method used to transform the single diffraction image to diffractograms has been extensively described elsewhere [28]. However, it is worthwhile to outline the main steps and indicate specific details used in the present study regarding the phase and texture analysis. The basic data analysis procedure consists of correcting the image by dark current, flat-field and spatial distortion corrections in order to obtain intensities that depend only

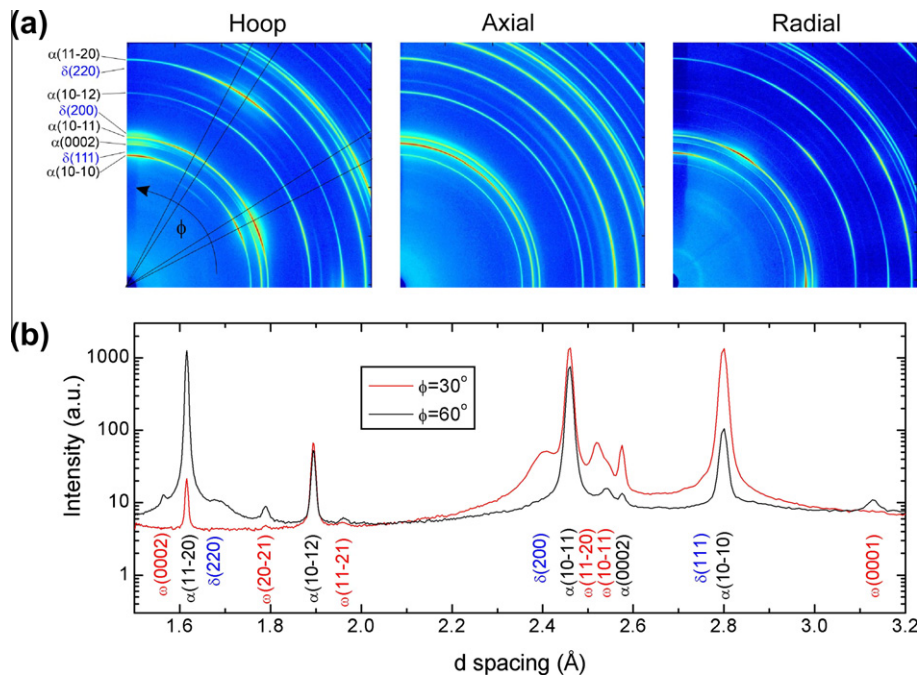


Fig. 2. (a) Typical images recorded by the area detector along the tube hoop, axial and radial directions, obtained with specimens C, B and D, respectively, indicated in Fig. 1. For better clarity, the color scheme is proportional to the logarithm of the counts, and only a quarter of the image is shown. Debye rings corresponding to α -Zr and δ -hydride have been indexed. (b) Diffractograms produced from the two azimuth sections ($27.5^\circ < \phi < 32.5^\circ$) and ($57.5^\circ < \phi < 62.5^\circ$) indicated in the hoop image. (For interpretation of the references to colour in this figure legend, the reader is referred to the web version of this article.)

on the sample and the diffraction geometry. After defining a center, the corrected image is transformed into a series of 2θ diffractograms, which are analyzed as conventional θ – 2θ scans. The Debye rings were divided into 72 azimuths (ϕ angle in the figure), so each diffractogram corresponds to an angular section with a width of 5° . Fig. 2b shows two diffractograms obtained from the hoop image for the two azimuthal sections indicated in Fig. 2a. The diffractograms are expressed in terms of d -spacing to aid the indexation of diffraction peaks. For all diffractograms, the position, integrated intensity and width of all the accessible peaks from the observed phases were determined by least-squares refinement using a pseudo-Voigt profile. Because of the marked crystallographic texture, the peak intensities change both around the ring and as a function of the incident beam orientation. So, the crystallographic textures of the α -Zr matrix and the δ -ZrH precipitates were determined through the study of such dependence. Specific details about the texture analysis will be addressed in the following section.

The local variations in phases and texture across the hydride blister were investigated by taking images of Debye rings at different locations of sample A. The X-ray beam was aligned with the hoop direction of the tube, as depicted schematically in Fig. 3a. Several lines on the radial–axial plane of the blister were scanned by translating the sample on the X – Y plane of the figure and taking images at selected locations. Two such lines are indicated in the figure. Line X scans the sample along the axial direction

for a fixed radial position, which was kept close to the surface of the sample. Line Y scans along the radial direction (depth profile), not far from the center of the blister. The size of the X-ray beam corresponds to the size of the color squares, discussed below.

4. Results

4.1. Hydride concentration in the blister

Fig. 3b presents diffractograms obtained at different positions of sample A: (a) outside the blister, (b) at the blister/matrix interface and (c) at its center. Hexagonal α -Zr is the main component outside the blister, with minor fractions of δ -ZrH and ω -Zr. The ω -Zr phase has a hexagonal structure and is the result of the decomposition of the metastable β -Zr phase (bcc) which remains after the tube extrusion performed in the $\alpha + \beta$ field at 817°C [29]. At the blister/matrix interface (~ 2 mm from the blister center), there is a marked increase in the δ -hydride phase and a decrease in α -Zr, while the ω -Zr phase seems to disappear. Two small shoulders appearing to the left of the $\delta(200)$ and $\delta(111)$ hydride peaks indicate the presence of a small quantity of γ -hydride. The δ -hydride phase is the main component at the blister center, but the α -Zr peaks are still important. The γ -hydride peaks are not easily distinguished at the blister center, presumably because they are masked by the broader δ -ZrH peaks. Provided only minor amounts of the γ -hydride and ω -Zr phases

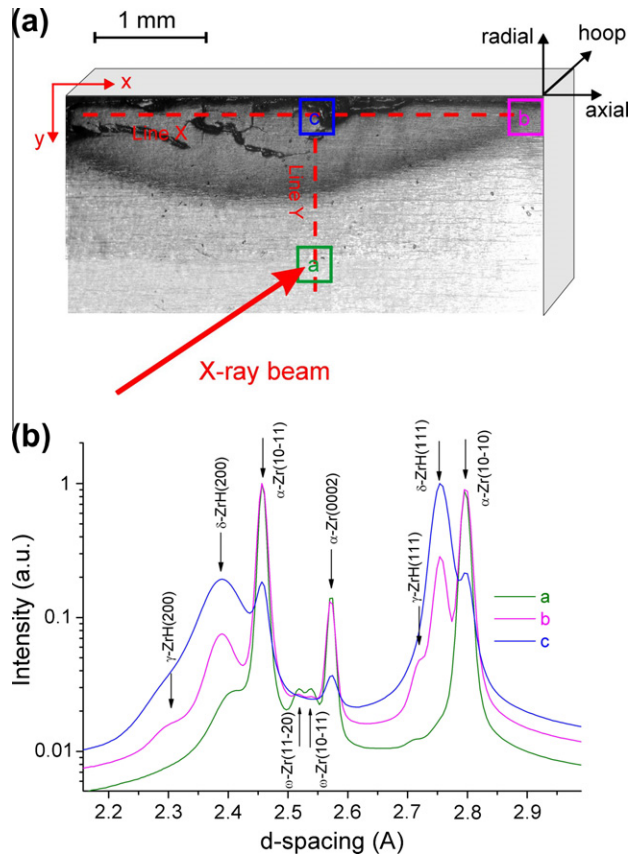


Fig. 3. Top: Representation of the spatially resolved experiments performed on sample A of Fig. 1, indicating the two lines (*X* and *Y*) scanned by the measurements. The color squares have the dimensions of the incident X-ray beam. Bottom: Average diffractograms obtained at locations a, b and c indicated in top figure. The main crystallographic phases for Zr (α , ω) and for the hydride (δ , γ) are indexed. (For interpretation of the references to colour in this figure legend, the reader is referred to the web version of this article.)

are present all through the specimen, they will not be considered in the quantitative phase analysis performed below.

A quantitative phase analysis can be performed by comparing the integrated intensities of the α -Zr and δ -hydride peaks [30]. In principle, quantification of phase volumes for the present material requires knowledge of the crystallographic texture of both phases, and such a texture analysis will be presented in the following section. Nevertheless, a quantitative profile of phase compositions across the blister can still be derived from the integrated peak intensities recorded at different locations, as long as the textures do not change through the sample. Quite surprisingly, only minor changes in texture were observed when scanning across the blister, suggesting that the texture of both phases is relatively independent of hydride content. This can be appreciated in Fig. 4a and b, which show, respectively, the variation in the intensities of the $\delta(111)$ and $\alpha(10\bar{1}0)$ peaks around the Debye rings, measured for different positions along line *X* indicated in Fig. 3a. The curves are plotted as functions of the azimuth angle ϕ around the ring, and have been normalized by the average intensity to aid comparison between different

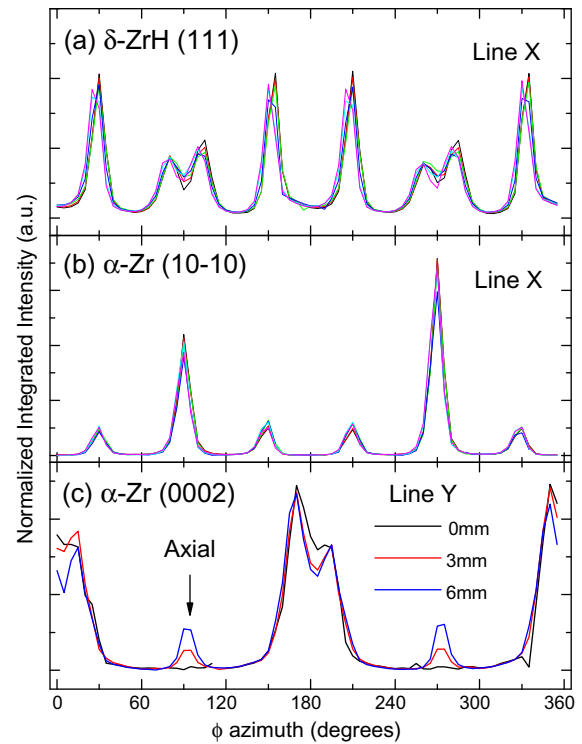


Fig. 4. Intensity variation around selected Debye rings, for different locations of the *X* and *Y* lines indicated in Fig. 3. The results have been normalized to aid comparison. Most rings displayed the same intensity distribution at all locations, as exemplified by figures (a) and (b). The only exception was the $\alpha(0002)$ ring measured at different depths.

hydride contents. All curves coincide, indicating that the texture is essentially the same for positions inside and outside the blister. The same behavior was observed for all diffraction rings of both phases at all positions, which means that hydride precipitation takes place equally in all grains. The only exception was observed for the $\alpha(0002)$ ring with the beam aligned to the hoop direction when measured along line *Y*, as shown in Fig. 4c. The figure indicates that there are a very small number of Zr crystallites with their *c*-axis aligned to the tube axial direction, which seems much more prone to hydride formation than the rest, a point to be discussed later in this section. However, as can be appreciated from Fig. 2a, those grains represent only a very minor fraction of the total, so they will be disregarded in the present phase analysis.

Provided texture is almost independent of sample position, the hydride X_{ZrH} and matrix X_{Zr} fractions can be straightforwardly evaluated ($X_{Zr} + X_{ZrH} = 1$). These fractions are proportional to the integral of the diffraction peaks over the ring, being the proportionality factor dependent on the phase and diffracting plane.

$$X_{Zr} = A_{Zr}^{i-peak} \cdot \langle I_{Zr}^{i-peak} \rangle$$

$$X_{ZrH} = A_{ZrH}^{j-peak} \cdot \langle I_{ZrH}^{j-peak} \rangle$$

Fig. 5 shows the hydride and α -Zr fractions for the two lines analyzed. Outside the blister, the hydride concentration was <0.03 , which corresponds to a concentration of

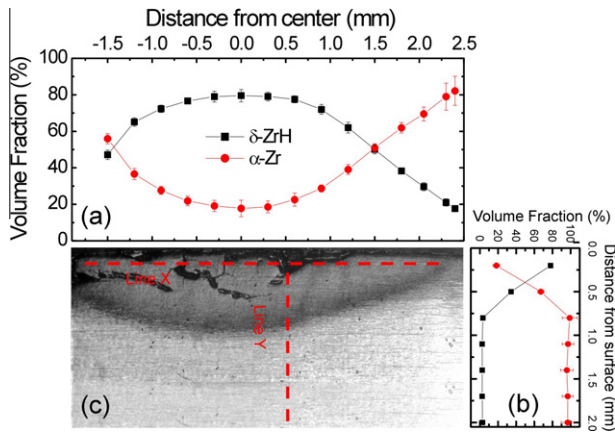


Fig. 5. (a) Near-surface and (b) through-depth profiles of phase volume fractions across the blister, for lines X and Y shown in (c).

290 wt.ppm of H in Zr. At the center of the blister the hydride fraction is ~ 0.8 , which indicates that, even after pressing the cold spot for 1650 h, there is not a complete transformation of α -Zr into hydride. The present is in contrast to simulations of the hydride blister formation, where the hydride fraction was predicted to be close to 1 within the blister [7,15].

4.2. Texture analysis

A detailed texture analysis of the crystallographic texture of both α -Zr and δ -hydride phases was performed for the pressure tube material far from the hydride blister. Full Debye rings were obtained for three sample orientations by aligning the incident X-ray beam with the hoop, axial and radial direction of samples A, B and C, respectively. Details of the rings are shown in Fig. 2a. Large variations in peak intensities are clear both from the images as well as from the diffractograms extracted at selected azimuth angles. As an example, the δ -(2 0 0) reflection is clearly observed in the diffractogram for the 30° azimuth shown in Fig. 2b, while it is absent in the 60° azimuth. The opposite happens for the δ -(2 2 0) reflection.

The traditional method of evaluating the crystallographic texture from X-ray diffraction involves the measurement of several complete or incomplete pole figures, and the subse-

quent determination of the ODF through a minimization method [31]. In the texture analysis performed here, the intensity variations around Debye rings are converted into incomplete pole figures. The ODF is then calculated from a least-squares refinement from a number of such incomplete pole figures. For the transmission geometry used in the present experiments, the Debye rings map into lines on the pole figure plots [32], with a one to one correspondence between a Debye ring and a line in the pole figure. Figures shown in Fig. 6 display the lines corresponding to the three sample orientations explored in the present experiments. The arrows in the figure indicate the direction of advance in the azimuth scan as the Debye rings is scanned. The dot placed at the beginning of the arrow corresponds to the 0° azimuth. The color of each dot is proportional to the number of counts registered at each angle, in this case showing the results for the α -Zr ($10\bar{1}0$) ring. Similar pole figures were obtained for all Debye rings accessible to the CCD camera. Seventy-two different orientations are explored by each Debye ring in the present analysis. The MTEX algorithm [33] was used to determine the ODF from the incomplete pole figures. The MTEX algorithm is based on a discretization of the angular ODF space by radially symmetric functions and on the fast spherical Fourier transform. The algorithm has proved to be particularly stable for very sharp textures with low symmetry.

4.3. α -Zr texture

Nine Debye rings were used to define the ODF of the α -Zr phase. This is equivalent to 1944 sample orientations, which is not far from the number of orientations typically explored in conventional measurements of pole figures (~ 2800). Fig. 7b shows the (0 0 0 1), ($10\bar{1}0$) and ($10\bar{1}1$) pole figures calculated from the experimentally determined ODF. The pole figures display the typical features observed in Zr–2.5%Nb pressure tubes [29]. A relatively high texture index (~ 7) gives a measure of the sharpness of this texture. The (0 0 0 2) basal planes present a pole along the hoop direction which elongates towards the radial direction, while the prismatic ($10\bar{1}0$) planes show a strong pole along the axial direction. This main texture component is clearly

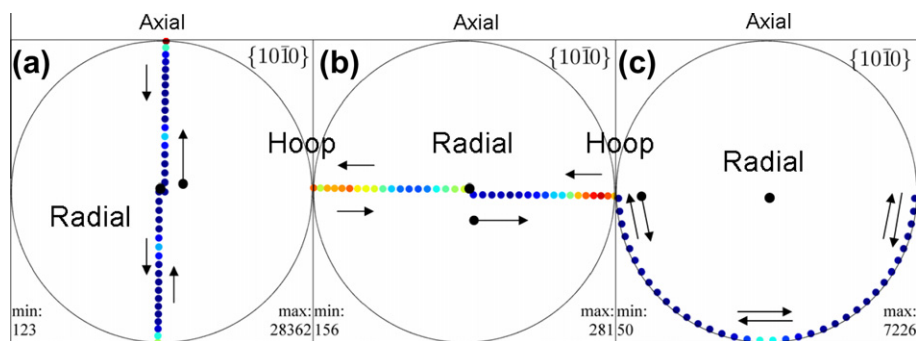


Fig. 6. Incomplete pole figures obtained from the variation in peak intensity around the Debye rings displayed in Fig. 2. The figures are for the incident X-ray beam along (a) hoop, (b) axial and (c) radial directions, respectively. The color of the symbols is proportional to the number of counts registered for α -Zr ($10\bar{1}0$) Debye ring. (For interpretation of the references to colour in this figure legend, the reader is referred to the web version of this article.)

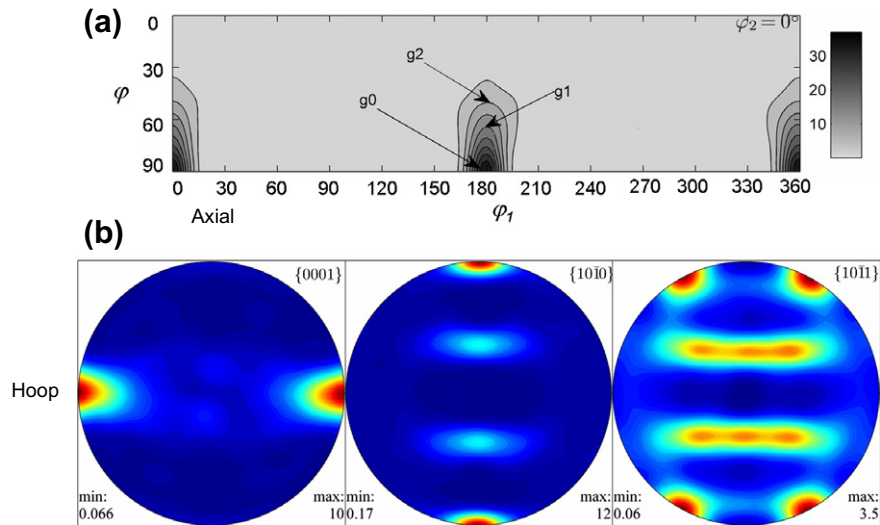


Fig. 7. Experimental texture of the pressure tube α -Zr phase. Top: $\varphi_2 = 0^\circ$ section of the ODF (Bunge notation). The arrows indicate the location of the ideal components discussed in the text. Bottom: Pole figures for selected reflections.

visualized in Fig. 7a, showing the $\varphi_2 = 0$ section of the ODF (Bunge notation). Most grains have their c -axis pointing to the hoop direction and their $[10\bar{1}0]$ axis parallel to the axial direction, which corresponds to the ~ 37 times random maxima found at $(\varphi, \varphi_1, \varphi_2) = (90^\circ, 0, 0)$ and $(180^\circ, 0, 0)$. Near these maxima, there are also a great number of grains with their $[10\bar{1}0]$ axis parallel to the axial direction, but with their c -axis rotated up to 45° from the hoop direction. These grains are responsible for the ellipsoidal shape of the ODF and of the elongated structure observed between the hoop and radial directions in the (0002) pole figure. The grains with their c -axis pointing to the radial direction ($\varphi = 0$) $\sim 1.4\times$ random is still higher than for a perfectly isotropic polycrystal.

A synthetic model of the α -Zr ODF was produced in order to identify the main texture components of the hydride phase presented below. The ODF is represented by three main component $g_0 = (90^\circ, 0, 0)$, $g_1 = (60^\circ, 0, 0)$ and $g_2 = (45^\circ, 0, 0)$, as shown in Fig. 7a. The last two orientations correspond to grains with their c -axis rotated 30° and 45° from the hoop direction, respectively. The frequency of appearance sharply decreases as φ departs from 90° ; in particular g_0 has $\sim 37\times$ random, $g_1 \approx 15$ and $g_2 \approx 7$.

4.4. δ -Hydride texture

Three Debye rings were used to define the ODF of the δ -hydride phase. Fig. 8b shows the (001) , (110) and (111) pole figures calculated from the experimentally determined ODF, while Fig. 8a shows two sections of the ODF, for $\varphi_2 = 0^\circ$ and $\varphi_2 = 45^\circ$ (Bunge notation). For simplicity, the ODF is presented assuming orthorhombic symmetry of the sample, but the calculations were done without this assumption. The most remarkable feature is the marked decrease in the intensity of the texture, manifested in a texture index of ~ 2.3 compared with the value ~ 7 found

for α -Zr. There could, however, be some concern about the uncertainty of the experimental ODF presented in Fig. 8, as only 648 sample orientations are explored by the three rings used in the present analysis. So for proper interpretation of these results, the ODF of the hydride phase was calculated from the ODF of the α -Zr phase by applying the orientation relationship between parent and precipitate crystals most widely reported in the literature [34], i.e., $\alpha(0001)//\delta(111)$ and $\alpha[11\bar{2}0]//\delta[110]$. The calculated ODF and pole figures are presented in Fig. 9. The calculation was done without imposing sample symmetry, but the ODF is shown assuming orthorhombic sample symmetry just to facilitate comparison with the experimental ODF presented in Fig. 8a. All components of the experimental ODF in Fig. 8a are well reproduced by the calculation shown in Fig. 9a: the three maxima in the $\varphi_2 = 0$ section and the two maxima in the $\varphi_2 = 45^\circ$ section. The calculated texture index is ~ 2.5 compared with the ~ 2.3 value given by the experiment. The good agreement between the theoretical and the experimental textures supports the method used for the determination of the experimental hydride texture. The authors believe that the high symmetry of the δ phase (cubic) allows a reasonable ODF to be obtained, even with scattered pole figures.

The description of the α -Zr ODF by three main texture components provides the basis for the interpretation of the hydride ODF. The arrows in Fig. 9a indicate the hydride texture components that result from the three α -Zr texture components introduced in Fig. 7a. These texture components are represented by circles of different colors in the pole figures in Fig. 9b. The hydrides precipitated in the α -Zr grains with the most frequent orientation (g_0) are responsible for the two maxima observed at the $\varphi_2 = 0$ and $\varphi_2 = 45^\circ$ sections, and almost all the features observed in the experimental pole figures. The other two components of the α -Zr phase (g_1 and g_2) also have their correspondences on the hydride texture: the

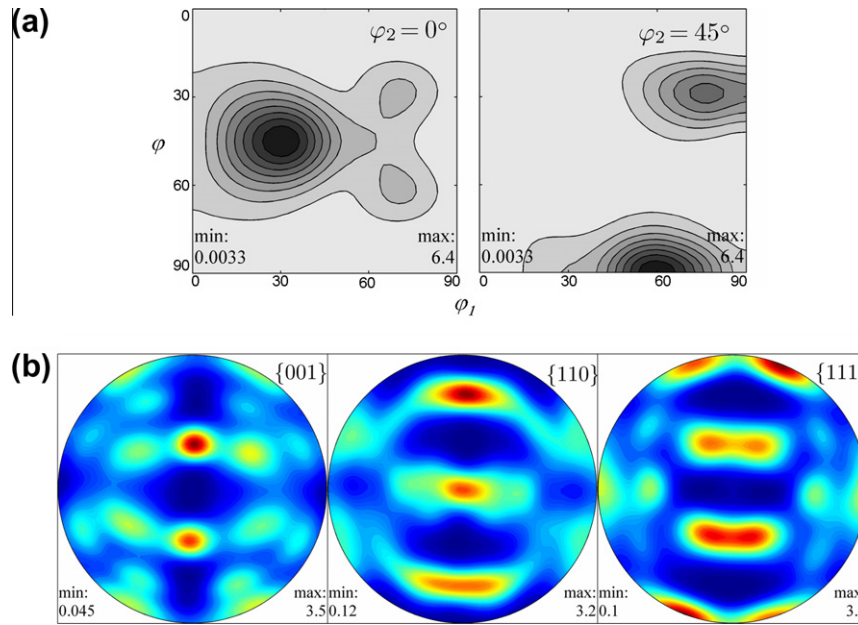


Fig. 8. Experimental texture of the δ hydrides precipitated in the pressure tube. Top: $\phi_2 = 0^\circ$ and $\phi_2 = 45^\circ$ sections of the ODF (Bunge notation). Bottom: Pole figures for selected reflections.

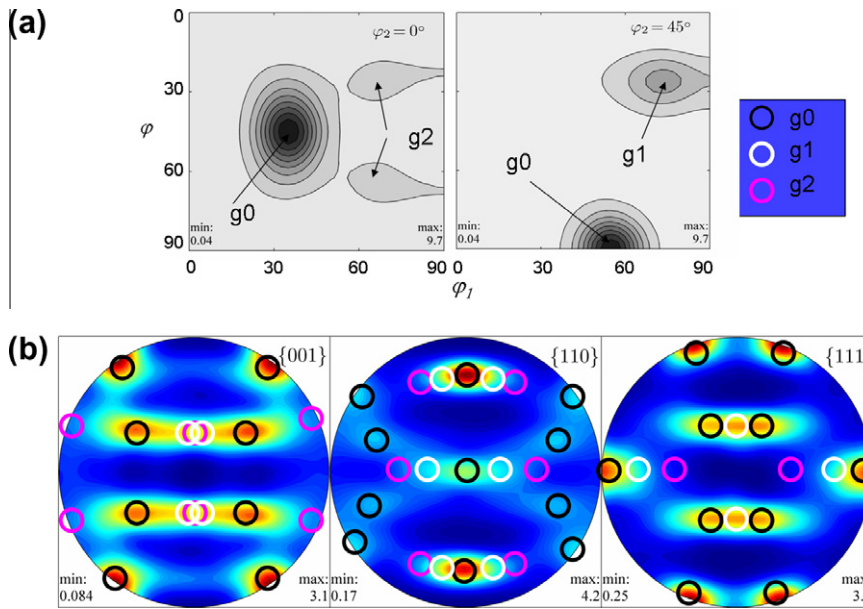


Fig. 9. Calculated texture of the δ hydrides precipitated in the pressure tube, obtained by applying the $\alpha(0001)/\delta(111)$ and $\alpha[1120]/\delta[110]$ orientation relationship to the α -Zr ODF presented in Fig. 7. Top: $\phi_2 = 0^\circ$ and $\phi_2 = 45^\circ$ sections of the ODF. The arrows indicate the location of the texture components resulting from the transformation of the ideal orientations indicated in Fig. 7. Bottom: Pole figures for selected reflections. The circles indicate the locations of the "ideal" texture components.

two other maxima at $\phi_2 = 0$ for g_2 and the maxima at $\phi_2 = 45^\circ$ for g_1 . The observed decrease in the texture index is explained by the cubic symmetry of the hydride phase and the matrix/precipitate relationship, which involves two precipitation variants. So, in the (1 1 1) pole figure in Fig. 8, several precipitates have their (1 1 1) poles near the axial–radial plane, despite the fact that the (0 0 0 1) pole figure in Fig. 7 indicates that only a small number of α -Zr crystals have their c -axis along these directions. As indicated by

the black circles in Fig. 9b, these precipitates actually result from α -Zr grains from g_0 , the main texture component.

Some minor differences are found between the experimental and calculated pole figures. The most relevant difference is the exacerbated intensification of the center of the two horizontal structures of the experimental (0 0 1) pole figure, which is not well reproduced by the calculation. It is worth mentioning that this peak is not an artifact from the analysis, since it can be observed as a maximum along

the $\delta(0\ 0\ 2)$ Debye ring for the measurement with the beam parallel to the hoop direction (see Fig. 2a).

5. Discussion

The profiles of hydride concentration measured across the blister showed a maximum volume fraction of 80% at the blister center, and a steady decrease in hydride concentration towards the edges over a length of ~ 2 mm (Fig. 5a). This decrease cannot be ascribed to the blurring introduced by the finite size of the experimental gauge volume (Fig. 3a), which is nearly an order of magnitude smaller than the extent of this hydride transition zone. These results are in qualitative agreement with the theoretical model of blister growth presented in [5], though in that work a maximum of 90% hydride volume was predicted at the blister center, and the decrease in hydride content developed over a much narrower range of ~ 0.3 mm. Larger disagreement is found with the model presented in Ref. [7], which predicts 100% hydride at the center and an even narrower transition zone. In both models of blister formation, a partially hydrided blister can effectively occur, depending on the interplay between H diffusion from the bulk into the cold zone, and the rate of hydride precipitation within the cold zone. The present results indicate that, although such numerical models of hydride blister growth can predict the evolution of blister size quite well, they may not capture precisely the hydride distribution that exists within the blister.

In view of this new information about the hydride distribution that exists within the blister, it is possible to reassess the models for the stress field around the blister. In accordance with the present experiments, the stress model developed by Wallace [12] allows for different degrees of blister hydriding. So for 100% transformation, the point in the blister with maximum hydride concentration corresponds to single-phase zirconium hydride, while at lower percentages the blister is always composed of a mixture of δ -hydride and α -Zr phases. Hence, the predictions for 75% transformation presented in Ref. [12] are considered to be the better description for a real hydride blister. However, as the adopted hydride distribution is much sharper than the one measured here, the model would overestimate the misfit stresses at the blister/matrix interface. This could partially explain the discrepancy between an experimental value of -300 MPa reported in Ref. [16] for the interface near the surface, and the value of -400 MPa predicted in Ref. [12]. This also explains the unrealistically large stress values predicted by Singh et al. [8], which does not allow for any gradient in hydride composition, i.e., 1100 MPa compared with 180 MPa given by Wallace. The comparison between the models and experiments is correct as long as the blister remains uncracked. As pointed out in Ref. [16], cracks usually appear within the blister as a mechanism for relaxation of the macroscopic stresses.

Regarding the texture analysis performed here, it was shown that the crystallographic texture measured for the hydrides in Zr–2.5%Nb pressure tubes can be reasonably

explained by the well-known crystallographic relationship between the α -Zr and δ -hydride lattices, namely $\alpha(0\ 0\ 1)//\delta(1\ 1\ 1)$ and $\alpha[1\ 1\ \bar{2}0]//\delta[1\ \bar{1}0]$. So, direct application of this transformation to the experimental α -Zr ODF (Fig. 7) gives an ODF for the hydride (Fig. 9) containing all the features present in the experimental hydride texture (Fig. 8). Moreover, this texture seems to hold for all hydrides in the pressure tube, i.e., both within the blister (where δ -hydride is the major phase) as well as in the bulk of the tube (where hydrides appear only as small precipitates). Provided hydrides are present in the sample over a wide range of concentrations, from 0.03 to 0.8 according to Fig. 5, this indicates that hydride texture is roughly independent of hydride concentration. So, these two separate observations provide a consistent first picture of hydride precipitation in Zr–2.5%Nb pressure tubes, on which the probability of hydride formation is very similar for the majority of α -Zr grains. This is an important conclusion, as such statistical information would be extremely hard to obtain by other experimental techniques. However, a more detailed examination of the experimental results reveals two departures from such a first approximation. First, detailed inspection of all Debye rings measured for all locations within the sample identified a small group of grains, i.e., those with their basal poles along the tube axial direction (Fig. 4c), which were clearly more prone to hydride formation than the rest. So this small texture component which is hardly visible in the $(0\ 0\ 1)$ pole figure of Fig. 7 completely disappeared from the α -Zr phase remaining within the blister. Performing scanning electron microscopy/electron backscatter diffraction experiments, Holt and Zhao [35] linked the microstructure and texture of Zr–2.5%Nb pressure tubes. They described the α -Zr ODF by three texture components with their c -axes along the tube axial, radial and hoop directions, respectively. They associated the axial texture component with colonies of Widmanstätten-like α -grains that are transformed from the β -phase. These grains have very low dislocation densities and are probably developed upon cooling after extrusion. This contrasts with the two main texture components, which have their basal poles preferentially aligned along the tube radial and hoop directions, respectively, corresponding to elongated grains that appear mainly due to slip-assisted deformation during extrusion. The higher affinity to hydride precipitation of grains in the axial texture component is possible associated with inter-granular stresses. Selective nucleation can occur on grains presenting a higher nucleation rate, as it could result from a favorable stress state which reduces the volume misfit involved in the phase transformation. In particular, it has been suggested that α grains with their c -axis stretched by the presence of tensile stresses should show an intensification of hydride precipitation [36]. So, an insight into the causes of selective nucleation can be gained by studying the stress state of the α -Zr material in the early stages of precipitation. This was done by studying the small distortions of the $\alpha(0\ 0\ 2)$ Debye rings. Fig. 10 shows the variation in the c -axis of the hexagonal lattice for α -Zr crystallites with different orientations relative to the tube

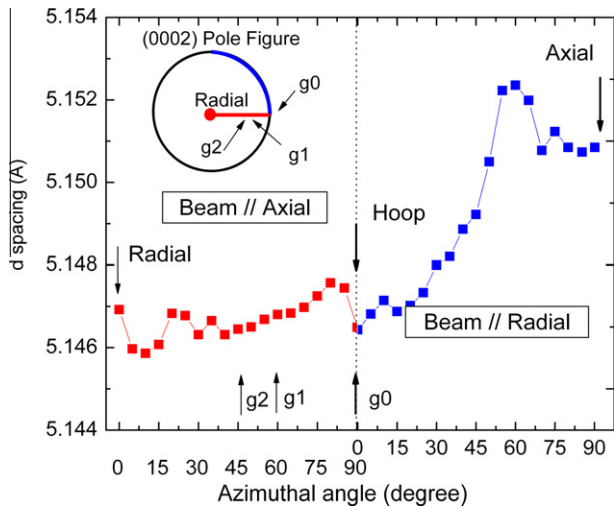


Fig. 10. Value of the α -Zr unit cell c -axis along different pressure tube directions. The x -axis gives the azimuthal angle in the original Debye ring. The inset displays the orientations explored by the experiment within a pole figure. Arrows on the top indicate the orientations corresponding to the pressure tube principal axes. Arrows on the bottom indicate the ideal orientations presented in Fig. 7.

principal axes. The red (left) and blue (right) curves correspond to the azimuths measured for samples B and D, i.e., with the X-ray beam aligned to the tube axial and radial directions, respectively. The inset shows the paths in the pole figure explored by the two experimental configurations. The top arrows in the figure indicate the crystallites aligned to the tube principal axes. The bottom arrows indicate orientations corresponding to the three crystallite orientations introduced in the synthetic model of the pressure tube ODF. It is clear that the distance between basal planes is larger for the axial texture component compared with the hoop and radial directions, in agreement with the behavior predicted in the literature [36]. The c -axis strain difference between crystals belonging to the g_0 , g_1 , g_2 to texture components and those in the axial component is $\sim 1000 \mu\epsilon$.

The second departure from a completely isotropic model for hydride precipitation can be appreciated after a detailed comparison of Figs. 8 and 9, showing the experimental and calculated pole figures, respectively, for the δ -hydrides. The two maxima found on the radial–axial plane of the (0 0 1) pole figure are not well reproduced by the calculation. A possible explanation for this discrepancy could be the precipitation of hydrides with a different orientation relationship with the α -Zr lattice. This is feasible, as different precipitation modes have been reported for inter-granular and intra-granular hydrides. Intra-granular hydrides are reported to precipitate mainly by the ‘bulk’ relationship adopted here, i.e., $\alpha(0001)//\delta(111)$ and $\alpha[11\bar{2}0]//\delta[110]$. However, transmission electron spectroscopy (TEM) observations [36] have revealed that the ‘bulk’ relationship holds for hydrides grown at $\alpha\omega$ and $\alpha\beta$ –Nb interfaces, while two other relations are found for hydrides grown at α – β interfaces: (i) $\alpha(20\bar{2}1)//\delta(111)$ and

$\alpha[\bar{1}\bar{1}26]//\delta[\bar{1}\bar{1}2]$; and (ii) $\alpha[\bar{1}\bar{1}26]//\delta[1\bar{1}4]$ and $\alpha(1\bar{1}01)3^\circ$ from $\delta(110)$. The pole figures resulting from these two orientation relationships were calculated, but none can account for the maxima observed in the (0 0 1) experimental pole figure. The former is just 8° from the ‘bulk’ relationship, so it cannot reproduce this feature. The latter, which corresponds to the case $\alpha(0001)//\delta(001)$ would imply the precipitation on grains with a very low frequency of appearance in the α -Zr ODF. These results are consistent with the phase analysis performed here, which indicated just a marginal presence of β -Zr.

A more plausible explanation for the two maxima observed in the hydride (0 0 1) pole figure assumes different affinities for hydride precipitation for g_0 , g_1 and g_2 ; the three texture components describing the α -Zr ODF. As observed from Figs. 8 and 9, the location of the experimental maxima in the (0 0 1) pole figure coincide with white and pink circles, which represent poles resulting from the transformation of the g_1 and g_2 texture components, respectively. Hence, in principle, the presence of the experimental poles can be explained by assigning a higher probability of transformation to these texture components. By contrast to the previous case, similar values of the c -axis were measured for all three texture components (Fig. 10), so the stress state within the grains is unlikely to be the reason for such difference in probability. Yet the selective nucleation of g_1 and g_2 grains over the g_0 grains could be related to the grain morphology or dislocation density. Holt and Zhao [35] described the hoop texture component, i.e., the g_0 component introduced here, as composed of elongated α -grains containing a low dislocation density in which the c -axis is oriented parallel to the long dimension of the alpha grains in radial–transverse section. In contrast, the g_2 component is closer to their radial texture component, which comprises elongated α -grains containing a high density of dislocations in which the c -axis is oriented at a relatively high angle to the long dimension of grains as viewed in transverse section. This difference in dislocation densities would suggest that the higher affinity of g_2 grains to transform would result from a much larger number of nucleation sites during a heterogeneous nucleation process. However, no significant differences in α peak widths were found, which should reflect such large differences in dislocation density. According to Perovic et al. [36], hydrides are prone to nucleate on grain boundaries with their habit plane parallel to the basal plane of the α matrix. Then, grains with their c -axis perpendicular to the grain long dimension will have a more extended grain boundary surface that is favorable for nucleation. The elongated grains have typical sizes of $0.5 \mu\text{m}$ (radial), $5 \mu\text{m}$ (hoop) and $20 \mu\text{m}$ (axial) [35], so a simple calculation shows that grains in the radial texture components would have ~ 10 times more surface favorable for nucleation than g_0 grains. Following this idea, there would be more hydride precipitation in grains with g_2 orientation than in those with g_1 orientation, and much more than with g_0 orientation. Hence, this ‘grain shape’ selectivity may be responsible

for the intensification of the hydride texture components observed in the experimental texture.

So more information about this departure from a perfectly isotropic transformation could be obtained from observation of the spatial distribution of the 20% volume of the remaining α -Zr phase. In particular, it is not known whether the α phase remains as very thin lamellae between the hydride laths observed by TEM [36] for low H contents; or as isolated grains with unfavorable geometry/orientation/stress for hydride precipitation.

6. Conclusions

X-ray synchrotron diffraction experiments revealed the profile of hydride concentration across a hydride blister grown on the surface of a Zr–2.5%Nb pressure tube. The blister is composed mainly of δ hydride and α -Zr phases, with very small contributions from the metastable γ hydride and ω -Zr phases. A steady decrease in hydride concentration from the center to the edges of the blister was observed, which is in qualitative agreement with theoretical models of blister growth. A maximum concentration of 80% hydride phase volume was found at the center of the blister surface, in disagreement with models that predict a single-phase hydride for that location.

Application of a novel algorithm to the experimental data also allowed a quantitative analysis of the crystallographic textures of the two major constituent phases, α -Zr and δ hydride. The study revealed that the hydride precipitates present at low hydrogen concentrations and the solid hydrides found at the blister center both display the same crystallographic texture. This means that neither the texture of the metal matrix nor that of the hydride is substantially modified by the formation of the blister.

The δ -hydride texture was successfully interpreted in terms of the α -Zr texture by direct application of the parent–precipitate relationship most widely reported in the literature, $\alpha(0\ 0\ 0\ 1)/\delta(1\ 1\ 1)$ and $\alpha[1\ 1\ -2\ 0]/\delta[1\ -1\ 0]$. Some selective precipitation on α -Zr grains with particular orientations was revealed by the intensification of specific texture components. Possible explanations for this selectivity were discussed in terms of tensile stresses in the c -axis of the Zr crystal, dislocation densities and the availability of grain boundaries favorable for hydride nucleation.

Acknowledgements

The authors wish to thank A. Motta, K. Colas, M.R. Daymond and M. Kerr for experimental help and fruitful discussions. This research was funded by a Pan-American Collaboration Program funded by CONICET, Argentina under Res 1161/07, with corresponding funding from NSERC and National Science Foundation for the Cana-

dian and American partners. Use of the Advanced Photon Source was supported by the US Department of Energy, under Contract No. DE-AC02-06CH11357.

References

- [1] Sawatzky A. J Nucl Mater 1960:321–8.
- [2] Field GJ, Dunn JT, Cheadle BA. Can Metall Q 1985:181.
- [3] Chung HM. Technical Report ANL/ET/CP-10004, Argonne National Laboratory; 2000.
- [4] Pierron ON, Koss DA, Motta AT, Chan KS. J Nucl Mater 2003:21–35.
- [5] Leger M, Moan GD, Wallace AC, Watson NJ. ASTM STP 1023. American Society for Testing and Materials; 1989. p. 50.
- [6] Puls MP. Metall Trans A 1988:2247–57.
- [7] Domizzi G, Enrique RA, Ovejero-Garcia J, Buscaglia GC. J Nucl Mater 1996:36–47.
- [8] Singh RN, Kishore R, Sinha TK, Kashyap BP. J Nucl Mater 2002:153–64.
- [9] IAEA-TECDOC-1410 2004.
- [10] Domizzi G, Vigna G, Bermudez S, Ovejero-Garcia J. J Nucl Mater 1999:255–67.
- [11] Vanderglas ML, Kim YJ. Int J Pres Vess Pip 1986:22–177.
- [12] Wallace AC. In: Transactions of the ninth international conference on structural mechanics in reactor tech; 1987. p. 87–92.
- [13] Singh RN, Kishore R, Sinha TK, Banerjee S, Kashyap BP. Mater Sci Eng A 2003:17–28.
- [14] Laursen T, Leger M, Ma Xin-Pei, Macarthur JD, Palmer GR, Whittton JL. J Nucl Mater 1989:156–63.
- [15] Byrne TP, Gadala TP, Leger M. In: Transactions of the Eight International Conference on Structural Mechanics in Reactor Technology, North-Holland, Amsterdam, The Netherlands; 1985.
- [16] Santisteban JR, Steuwer A, Domizzi G, Peel M. Powder Diffraction 2009:S72–6.
- [17] Carpenter GJC. J Nucl Mater 1973:264–6.
- [18] Barraclough KG, Beevers CJ. J Nucl Mater 1970:125–34.
- [19] Barraclough KG, Beevers CJ. J Mater Sci 1969:518–25.
- [20] Puls MP, Shi San-Qiang, Rabier J. J Nucl Mater 2005:73–80.
- [21] Kerr M, Daymond MR, Holt RA, Almer JD, Stafford S, Colas KB. Scripta Mater 2009:939–42.
- [22] Steuwer A, Daniels JE, Peel MJ. Scripta Mater 2009:431–3.
- [23] Kerr M, Daymond MR, Holt RA, Almer JD, Stafford S. Scripta Mater 2010:341–4.
- [24] Colas KB, Motta AT, Chu YS, Almer JD, Daymond MR, Kerr M, et al. Acta Mater 2010:6575–83.
- [25] Santisteban JR, Vicente Alvarez MA, Viscaino P, Banchick AD, Almer JD. Acta Mater 2010:6609–18.
- [26] Steuwer A, Santisteban JR, Preuss M, Peel MJ, Buslaps T, Harada M. Acta Mater 2009:145–52.
- [27] Kerr M, Daymond MR, Holt RA, Almer JD. J. Nucl Mater 2008:70–5.
- [28] Haefner DR, Almer JD, Lienert U. Mater Sci Eng A 2005:120–7.
- [29] Holt RA, Aldridge SA. J Nucl Mater 1985:246–59.
- [30] Daum RS, Chu YS, Motta AT. J Nucl Mater 2009:453–63.
- [31] Bunge H-J. Texture Analysis in Materials Science. London: Butterworths; 1982.
- [32] Wenk H-R, Grigull S. J Appl Cryst 2003:1040–9.
- [33] Hielscher R, Schaeben H. J Appl Cryst 2008:1024–37.
- [34] Bradbrook JS, Lorimer GW, Ridley N. J Nucl Mater 1972:142–60.
- [35] Holt RA, Zhao P. J Nucl Mater 2004:520–8.
- [36] Perovic V, C Weatherly G, Simpson CJ. Acta Metall 1983: 1381–91.